

The following publication Wu, Y., Wu, J., & Wong, W. Y. (2021). A new near-infrared phosphorescent iridium (III) complex conjugated to a xanthene dye for mitochondria-targeted photodynamic therapy. *Biomaterials Science*, 9(14), 4843-4853 is available at <https://doi.org/10.1039/d1bm00128k>.

A new near-infrared phosphorescent iridium(III) complex conjugated to an xanthene dye for mitochondria-targeted photodynamic therapy

Yongquan Wu,^{a,b,c} Jie Wu^c and Wai-Yeung Wong^{a,b,*}

Iridium(III) complexes are potent candidates for photodynamic therapy (PDT), but some key drawbacks still hamper clinical translation, such as poor operability in the phototherapeutic window, high darktoxicity, and low reactive oxygen species (ROS) production efficiency. In this work, a near-infrared phosphorescent Ir(III) complex conjugated to an xanthene dye, NIR-Ir-XE, is reported with highly favourable properties for mitochondria-targeted imaging and cancer phototherapy. The generation of the triplet excited state of an xanthene moiety endows the NIR-Ir-XE to form singlet oxygen ($^1\text{O}_2$) for use as a photodynamic therapy agent after irradiation with visible light. Compared with the xanthene-free Ir(III) counterpart (NIR-Ir-bpy), the xanthene-modified cyclometalated Ir(III) photosensitizer NIR-Ir-XE exhibits higher $^1\text{O}_2$ generation efficiency, negligible dark toxicity and better therapeutic effect. Importantly, a clear correlation between cell death and intracellular generation of $^1\text{O}_2$ derived from NIR-Ir-XE after light irradiation was demonstrated. The corresponding *in vivo* photo-antitumor performance was further demonstrated to be effective in tumor-bearing mice. The observed properties of NIR-Ir-XE qualify it as a promising PDT agent.

1. Introduction

Photodynamic therapy (PDT) has attracted great attention recently, which uses light and photosensitizers to generate reactive oxygen species (ROS) to specifically kill cancer cells.^[1, 2] It has many advantages such as noninvasive nature, low treatment resistance, high controllability, and high specificity compared with the traditional surgery, chemotherapy, and radiotherapy.^[3, 4] There are two kinds of PDT modality, in which type II method converts molecular oxygen into cytotoxic singlet oxygen ($^1\text{O}_2$).^[5] The key element for PDT is that highly cytotoxic reactive oxygen species (ROS) generated by the photosensitizers (PSs) upon light irradiation lead to cell apoptosis and necrosis.^[6, 7] Herein, an excellent PS is crucial for the therapeutic efficacy of PDT.

There have been a number of efforts devoted to the development of ideal photosensitizers for PDT.^[8-10] At present, most PSs for PDT are based on organic dyes, including boron dipyrromethene (BODIPY), porphyrin, and their derivatives.^[11-13] However, the reported PSs possess several drawbacks: (I) the relatively low efficiency of $^1\text{O}_2$ production results in high dosage and longer irradiation time; (II) the poor water

solubility and stability severely hinder their application; (III) the lack of organelle-targeting ability induces a poor therapeutic efficacy in real application. In order to fulfill the criteria of a large molar extinction coefficient, high intersystem crossing (ISC) efficiency, and good photostability, an effective method for improving the efficiency of singlet oxygen generation is to accelerate the ISC by introducing heavy atoms into PSs, such as halogens, transition metals, etc.^[14-19] Especially, cyclometalated Ir(III) complexes have gained attention as promising photosensitizers in PDT because of their ideal photophysical properties, large Stokes shift, and high ISC ability.^[20-33]

On the other hand, the xanthene dye, one of the most common organic dyes, has been widely applied in chemosensors and biomolecules.^[34, 35] Xanthene dyes have excellent photophysical properties, such as high fluorescence quantum yields, high molar extinction coefficients, good water solubility, high tolerance to photobleaching, and high mitochondrial-targeting ability.^[36, 37] Recently, some research works in the combination of xanthene dyes with transition metal systems demonstrate the promising applications in photosensitization, chemosensor, and bioimaging.^[38-40] In particular, a living biological system is a complex environment that can cause short-lived autofluorescence and tissue scattering during bioimaging.^[41] However, equipping the PSs with NIR-emitting property can overcome the problem, allowing it to have deeper tissue penetration, low photo-damage, and minimal background fluorescence.^[42, 43] Therefore, exploitation of a NIR-emitting PS for both high

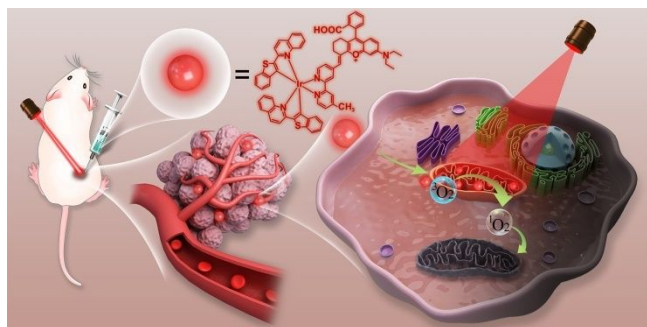
^a Department of Applied Biology and Chemical Technology, The Hong Kong Polytechnic University, Hung Hom, Hong Kong, P. R. China, E-mail: wai-yeung.wong@polyu.edu.hk

^b The Hong Kong Polytechnic University Shenzhen Research Institute, Shenzhen 518057, P. R. China

^c Key Laboratory of Organo-Pharmaceutical Chemistry of Jiangxi Province, Gannan Normal University, Shiyuan South Road, Ganzhou 341000, P. R. China

signal-to-noise (SNR) imaging and PDT still need to be further developed.

With these considerations, we envisaged that xanthene dyes are promising candidates for developing novel fluorescent PDT agents in combination with highly potent cyclometalated Ir(III) complexes. Herein, we fabricated a new hybrid system based on a NIR-emitting cyclometalated Ir(III) complex conjugated to an xanthene dye for mitochondrial-targeting imaging and PDT, which combines both imaging and therapeutic performances within one platform (Scheme 1). In this hybrid system, the collection of their respective merits from xanthene dyes and Ir(III) complexes was anticipated to provide a synergistic effect in the application of imaging and PDT. Moreover, the biological evaluation of a potential PS agent that integrates an Ir(III) complex with a representative xanthene dye demonstrates a good correlation between cell death and the production of $^1\text{O}_2$, which can be selectively generated after visible-light irradiation. Thanks to the unique features of cell imaging and PDT effect, we hope that this concept would not only have promising potential in organelle-targeting application, but also open up a new perspective in cancer treatment by PDT.



Scheme 1. Chemical structure of NIR-Ir-XE and its application for mitochondria-targeting photodynamic therapy in vivo.

2. Experimental section

2.1 Materials

All chemical reagents were purchased from commercial suppliers and used without further purification. 2-Chloroquinoline, 2-benzothienylboronic acid, cyclohexanone, 2-(4-diethylamino-2-hydroxybenzoyl) benzoic acid, and 4-formyl-4'-methyl-2,2'-bipyridine (P) were purchased from Shanghai Energy Chemical Co., Ltd (China). $\text{IrCl}_3 \cdot 3\text{H}_2\text{O}$ and tetrakis(triphenylphosphine)palladium(0) were purchased from Shanxi Rock New Material Co., Ltd (China). Tris-(2,2'-bipyridyl)-ruthenium(II) chloride hexahydrate, K_2CO_3 , NH_4PF_6 , H_2SO_4 , perchloric acid, acetic acid, 9,10-anthracenediylbis(methylene)dimalonic acid (ABDA), ascorbic acid, and rose bengal were purchased from Aladdin Technology Co., Ltd (China).

3-(4,5-Dimethyl-2-thiazolyl)-2,5-diphenyl-2-H-tetrazoliumbromide (MTT), phosphate buffered saline (PBS), Mito-Tracker Green, Mito-Tracker Red, Annexin V-FITC (fluorescein isothiocyanate), and propidium iodide (PI) were purchased from Jiangsu Beyotime Biotechnology Co., Ltd (China). Dichlorofluorescein diacetate (DCF-DA) was purchased

from Innochem Co., Ltd (China). Fetal bovine serum (FBS), JC-1 dye, and RPMI 1640 were purchased from ThermoFisher Scientific Co., Ltd.

2.2 Instruments

^1H NMR and ^{13}C NMR spectra were recorded on a Bruker DRX-400 NMR spectrometer (Germany) with tetramethylsilane (TMS) as an internal standard. High resolution mass spectra (HRMS) were obtained with an ESI ionization sources on Agilent 6540 mass spectrometer (USA). UV-Vis absorption spectra were obtained on Shimadzu UV-2700 spectrophotometer (Japan). Emission spectra were recorded on Agilent fluorescence spectrophotometer (USA). Luminescence lifetimes were detected using FLS980 steady-state/transient-state fluorescence spectrophotometer (UK). Daylight xenon light source CEL-S150 was purchased from CEALIGHT Co., Ltd (China). Cell imaging experiments were carried out using Olympus FV1000 laser scanning confocal microscopy (Japan). The absorbance values in MTT assay were measured using a Varioskan LUX microplate reader purchased from Thermo Fisher Scientific Inc (USA).

2.3 Synthesis

2.3.1 Synthesis of 2-benzothiophenylquinoline (btpq)

A mixture of 2-chloroquinoline (0.811 g, 5mmol), 2-benzothiophenylboronic acid (0.892 g, 5mmol), K_2CO_3 (2.072 g, 15mmol), tetrakis(triphenylphosphine)palladium(0) (0.462 g, 0.4mmol) and THF/ H_2O (40 mL, v/v = 1/1) was refluxed with stirring for 15 h under a N_2 atmosphere at 75 °C. After it was cooled, the mixture was poured into water and extracted with dichloromethane (15 mL \times 3). The combined organic phases were dried over anhydrous Na_2SO_4 , filtered and evaporated to dryness. The crude product was purified by using column chromatography with hexane/dichloromethane (v/v = 8/1) as the eluent. A white solid, 1.019 g (83.7%). ^1H NMR (400 MHz, CDCl_3) δ 8.16 (dd, J = 12.3, 8.6 Hz, 2H), 7.99 – 7.87 (m, 3H), 7.87 – 7.76 (m, 2H), 7.76 – 7.68 (m, 1H), 7.52 (t, J = 7.4 Hz, 1H), 7.37 (dd, J = 6.0, 3.1 Hz, 2H). ^{13}C NMR (101 MHz, CDCl_3) δ 152.32, 148.16, 145.54, 141.20, 140.48, 136.57, 129.95, 129.50, 127.51, 126.56, 125.33, 124.53, 124.30, 122.63, 122.43, 117.83. HR-MS: $\text{C}_{17}\text{H}_{11}\text{NS}$, $[\text{M}+\text{H}]^+$ calcd. 262.0690; found, 262.0577.

2.3.2 Synthesis of XE-P

Compound XE was synthesized according to the literature report.^[44] Cyclohexanone (3.3 mL, 32 mmol) was added dropwise to concentrated H_2SO_4 (50 mL) and cooled down to 0 °C. Then, 2-(4-diethylamino-2-hydroxybenzoyl)benzoic acid (5.01 g, 16 mmol) was added in portions with vigorous stirring. The reaction mixture was heated at 90 °C for 2 h, cooled down, and poured into ice (200 g). Perchloric acid (70%, 3.5 mL) was then added, and the resulting precipitate was filtered off and washed with cold water (200 mL). Compound XE obtained as a red solid was used for the next step without further purification.

Into a 50 mL flask were added compound XE (0.188 g, 0.5 mmol), compound P (0.100 g, 0.5 mmol), potassium acetate (0.147 g, 1.5 mmol) and acetic acid (3 mL). The mixture was heated to 70°C for 12 h under nitrogen protection, and the

solvent was removed by evaporation under the reduced pressure. The crude product was purified by silica gel chromatography (CH₂Cl₂/MeOH, v/v=40/1) to afford 105 mg of XE-P as a purple solid (37.7%). ¹H NMR (400 MHz, CD₃OD) δ 8.72 (s, 1H), 8.53 (d, *J* = 4.7 Hz, 1H), 8.45 (s, 1H), 8.30 – 8.17 (m, 2H), 8.06 (s, 1H), 7.83 – 7.68 (m, 2H), 7.62 (d, *J* = 4.4 Hz, 1H), 7.40 – 7.26 (m, 2H), 7.20 (d, *J* = 11.3 Hz, 2H), 7.09 (d, *J* = 9.2 Hz, 1H), 3.72 (d, *J* = 7.0 Hz, 4H), 3.00 (s, 2H), 2.50 (s, 3H), 2.37 (s, 2H), 1.82 (s, 2H), 1.33 (t, *J* = 7.0 Hz, 6H). ¹³C NMR (101 MHz, CD₃OD) δ 158.31, 155.82, 149.25, 148.56, 144.82, 133.45, 132.51, 130.19, 130.09, 129.87, 127.81, 125.15, 124.17, 122.34, 121.73, 117.26, 95.46, 45.76, 43.73, 26.56, 25.20, 21.22, 19.89, 11.49. HR-MS: C₃₆H₃₄N₃O₃⁺, [M]⁺ calcd. 556.2595; found, 556.2611. The purity was determined by HPLC analysis (Waters Alliance, USA) on SHIMSEN Ankylo C18 column (CH₃OH/CH₃CN = 95/5, 1 mL/min), λ = 300 nm, t_{major} = 1.19 min, t_{minor} = 2.26 min, purity: 95.12%.

2.3.3 Synthesis of complex NIR-Ir-XE

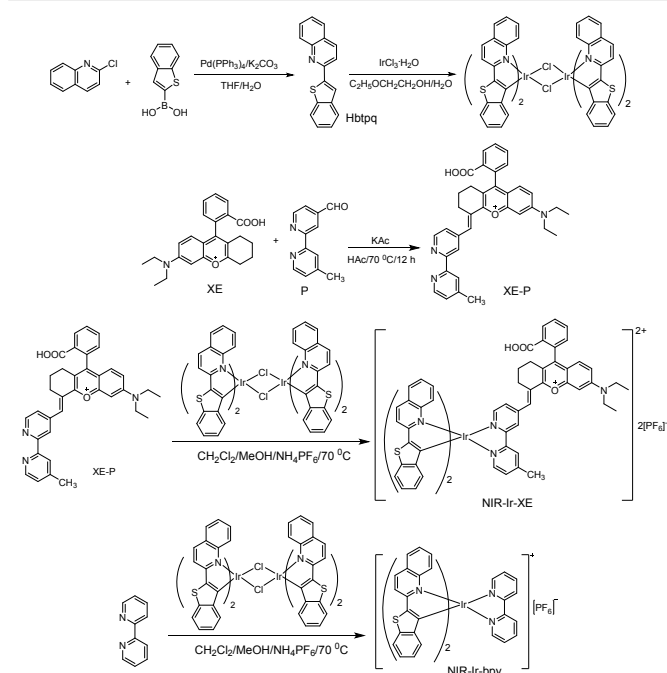
A mixed solvent of 2-ethoxyethanol and water (40 mL, v/v=3/1) was added to a flask containing IrCl₃·3H₂O (0.354 g, 1.0 mmol) and ligand btpq (0.535 g, 2.05 mmol). The mixture was refluxed for 24 h under a N₂ atmosphere, and filtered to obtain the cyclometalated iridium(III) chloro-bridged dimeric intermediate (btpq)₂IrCl₂Ir(btpq)₂. Brown solid, 0.612 g (40.9%).

A mixed solvent of CH₂Cl₂ and CH₃OH 40 mL (v/v = 1/1) was added to a flask containing (btpq)₂IrCl₂Ir(btpq)₂ (0.095 g, 0.064 mmol), and XE-P (0.072 g, 0.128 mmol). The mixture was refluxed for 12 h under a N₂ atmosphere at 75 °C. After it was cooled, NH₄PF₆ (0.042 g, 0.25 mmol) was added to the mixture, and then stirring was continued for 2 h. The crude product was purified using column chromatography with dichloromethane/methanol (v/v = 25/1) as the eluent. Brown solid, 32 mg (29.4%). ¹H NMR (400 MHz, CD₃OD) δ 8.44 – 8.34 (m, 3H), 8.24 (d, *J* = 5.3 Hz, 2H), 8.15 (d, *J* = 7.0 Hz, 1H), 8.11 – 8.00 (m, 3H), 7.87 (d, *J* = 8.1 Hz, 2H), 7.80 (d, *J* = 7.9 Hz, 2H), 7.69 (dt, *J* = 26.2, 7.5 Hz, 3H), 7.57 – 7.45 (m, 2H), 7.31 (t, *J* = 7.3 Hz, 2H), 7.16 (dt, *J* = 15.5, 7.5 Hz, 5H), 7.00 – 6.90 (m, 2H), 6.77 – 6.65 (m, 3H), 6.60 (t, *J* = 7.7 Hz, 2H), 6.34 (d, *J* = 8.3 Hz, 2H), 3.49 (q, *J* = 6.9 Hz, 4H), 2.69 (s, 2H), 2.46 (d, *J* = 5.6 Hz, 3H), 1.96 (d, *J* = 19.6 Hz, 2H), 1.68 (s, 2H), 1.19 (t, *J* = 6.8 Hz, 6H). ¹³C NMR (101 MHz, CDCl₃) δ 169.49, 166.75, 156.17, 155.51, 153.63, 153.28, 153.14, 152.87, 148.85, 148.64, 146.85, 146.65, 143.23, 143.19, 141.01, 140.93, 140.18, 140.13, 137.89, 134.52, 131.57, 131.43, 129.77, 129.39, 129.29, 128.87, 128.73, 126.81, 126.56, 126.44, 126.19, 125.71, 124.71, 123.73, 123.15, 118.22, 118.11, 31.81, 29.85, 27.66, 26.41, 23.44, 21.98, 21.27, 14.28, 12.46. HR-MS: C₇₀H₅₄IrN₅O₃S₂⁺, [M]⁺ calcd. 1269.3292; found, 1269.3236 (*z* = 1) and 634.6660 (*z* = 2).

2.3.4 Synthesis of complex NIR-Ir-bpy

A mixed solvent of CH₂Cl₂ and CH₃OH (30 mL, v/v = 1/1) was added to a flask containing (btpq)₂IrCl₂Ir(btpq)₂ (0.075 g, 0.05 mmol), and 2,2'-bipyridine (0.016 g, 0.1 mmol). The mixture was refluxed for 6 h under a N₂ atmosphere at 70 °C. After it was cooled, KPF₆ (0.045 g, 0.25 mmol) was added to the mixture, and then the mixture was stirred for 2 h. The crude product was purified by using column chromatography with dichloromethane/methanol (v/v = 20/1) as the eluent. Orange

solid, 42 mg (82.8%). ¹H NMR (400 MHz, DMSO-*d*₆) δ 8.57 (d, *J* = 8.7 Hz, 2H), 8.41 (d, *J* = 8.2 Hz, 2H), 8.32 (d, *J* = 5.5 Hz, 2H), 8.22 (d, *J* = 8.5 Hz, 2H), 8.13 (t, *J* = 7.8 Hz, 2H), 8.02 (d, *J* = 8.1 Hz, 2H), 7.93 (d, *J* = 8.1 Hz, 2H), 7.83 – 7.68 (m, 2H), 7.35 (s, 2H), 7.18 (t, *J* = 7.6 Hz, 2H), 7.06 – 6.88 (m, 4H), 6.79 – 6.60 (m, 2H), 6.21 (d, *J* = 8.4 Hz, 2H). ¹³C NMR (101 MHz, DMSO-*d*₆) δ 166.74, 155.64, 152.26, 148.58, 148.28, 146.56, 143.22, 142.32, 141.13, 140.59, 131.82, 130.19, 129.47, 127.33, 126.90, 126.62, 125.86, 125.14, 124.83, 124.11, 123.59, 119.12. HR-MS: C₄₄H₂₈IrN₄S₂⁺, [M]⁺ calcd. 869.1385; found: 869.1512 [M]⁺.



Scheme 2. Synthetic routes of XE-P, NIR-Ir-bpy, and NIR-Ir-XE.

2.4 UV–Vis absorption and emission spectra

The two kinds of spectra were measured with 1.0 cm quartz cells. The absorption spectra in solution were tested from 250 to 900 nm. The emission spectra were measured at λ_{ex/em} = 460/480 – 850 nm for compound XE-P, and λ_{ex/em} = 500/550 – 850 nm for complexes NIR-Ir-bpy and NIR-Ir-XE.

The luminescence quantum yields were measured using tris-(2,2'-bipyridyl)-ruthenium(II) chloride hexahydrate (Φ = 0.063 in DMF) as a standard and were calculated according to the equation: Φ_μ = Φ_sI_μA_sN_μ²/I_sA_μN_s², where N is the refractive index of the solvent, I is the integrated area of emission intensity, A is the absorbance at the excitation wavelength, and the subscripts μ and s refer to the reference sample and the sample, respectively.

2.5 Computational details

The iridium complexes were optimized by density functional theory (DFT) using the PBE functional (B3LYP), a functional that has been widely employed in the previous studies of iridium complexes.^[45] The “double-ζ” quality basis set LANL2DZ and the corresponding effective core potentials were used for iridium atom, while the 6-31G (p, d) basis set was used on non-metal atoms in the gradient optimizations.^[46, 47] The excited states of

S_1 and T_1 energies of the molecules were calculated by time-dependent density functional theory (TD-DFT).^[48] All the calculations were performed by the Gaussian 09 (Revision D.01).

2.6 Quantum yields for 1O_2 generation

To evaluate the triplet excited state lifetime of NIR-Ir-XE, transient absorption spectrum of NIR-Ir-XE in degassed toluene was acquired on an Edinburgh LP 980. A Nd: YAG laser 355 nm was used as the excitation source.

The 1O_2 quantum yields of the Ir(III) complexes in water were given by $\Phi_{PS} = \Phi_{RB}K_{PS}A_{RB}/K_{RB}A_{PS}$, where K_{PS} and K_{RB} are the decomposition rate constants of ABDA by the Ir(III) complexes and commercial rose bengal (RB), respectively. A_{PS} and A_{RB} represent the light absorbed by the Ir(III) complexes and RB, respectively, which are determined by integration of the areas under the absorption bands in the wavelength range of 400 – 800 nm. Φ_{RB} is the 1O_2 quantum yield of RB, which is 0.75 in water.

2.7 Electron spin resonance (ESR) assay

All measurements were carried out on an ADANI SPINSCANX spectrometer at 298 K. The spin adducts of the complex NIR-Ir-XE were detected by using the following conditions: 1 G field modulation, 20 mW microwave power, and 100 G-scan range. The spin trap 2,2,6,6-tetramethyl-4-piperidinol (100 mM) for trapping 1O_2 was applied. The ESR signals of the NIR-Ir-XE (10 μ M) before and after light irradiation (400–800 nm, 50 mW cm^{-2}) were tested.

2.8 Cell culture and cytotoxicity assay

MCF-7 cells (Michigan Cancer Foundation-7) were provided by the Institute of Biochemistry and Cell Biology (Chinese Academy of Sciences). Cytotoxicity tests were measured by *in vitro* MTT colorimetry. Logarithmic phase of MCF-7 cells was seeded into a 96-well flat-bottomed microplate (1×10^4 cells/well, 100 μ L well $^{-1}$), and then cultured in RPMI 1640 at 37 °C under 5% CO_2 atmosphere for 24 h. All media were also supplemented with 100 mg/mL of penicillin and 100 mg/mL of streptomycin.

Fresh nutrient solution (100 μ L/well) and different concentrations of NIR-Ir-XE solution (0, 1, 5, and 10 μ mol/L, diluted in RPMI 1640 nutrient solution, 100 μ L/well) were added and incubated for another 4 h in the dark. After that the cells were irradiated with 400–800 nm light (100 mW/ cm^2) for 1, 5, and 10 min, respectively. Then, the cells were incubated in the dark for a further 24 h. Next, 20 μ L MTT solution (5 mg/mL) was added to each well, and the cells continued to be incubated for 5 h under the same conditions. At last, the former mixed solution was discarded and 150 μ L DMSO was added into every well. The microplate was oscillated for 5 minutes to ensure that the formazan crystals fully dissolved. The absorbance value of each well at 570 nm was measured by microplate reader. Cell viability (%) = (mean of Abs. value of treatment group/mean of absorbance value of control group) \times 100%.

2.9 Intracellular localization of NIR-Ir-XE

Co-localization imaging. MCF-7 cells were incubated with NIR-Ir-XE (5 μ M) in RPMI 1640 medium at 37 °C for 30 min. For co-localization study, cells were washed with PBS, and 100 nM of Mito-Tracker Green FM (MTG) was added and incubated at 37 °C for 30 min. After washing with PBS for 3 times, the cells were imaged by Olympus FV1000 laser scanning confocal microscope. For NIR-Ir-XE, the excitation was 532 nm, and the band filter was 630 – 730 nm; for MTG imaging, the excitation wavelength was 488 nm, and the emission filter was 505 – 550 nm.

Photostability for NIR-Ir-XE in cell imaging. MCF-7 cells were incubated with NIR-Ir-XE (5 μ M) in RPMI 1640 medium at 37 °C for 30 min, and then the cells stained with NIR-Ir-XE were subjected to photobleaching study by confocal microscopy, the excitation wavelength was 515 nm, and the band filter was 620 – 720 nm. In the control group, MCF-7 cells were incubated with Mito-Tracker Red (MTR) (200 nM) in RPMI 1640 medium at 37 °C for 30 min, and then the imaging procedure was similar to the condition of NIR-Ir-XE-stained cell imaging. For MTR imaging, the excitation wavelength was 488 nm, and the emission filter was 600 – 650 nm. Photostability test was performed by using 515 nm laser with 40 mW output power as the irradiation source.

2.10 ROS detection in MCF-7 cells

The ROS generation in MCF-7 cells was measured by DCF-DA staining. MCF-7 cells were seeded in a 6-well plate and cultured for 12 h at 37 °C. Then, MCF-7 cells were incubated with NIR-Ir-XE (5 μ M) for 2 h and treated with DCF-DA (2 μ M) at 37 °C for 30 min. Thereafter, the cells were washed with fresh medium for three times followed by irradiation with a xenon lamp (400 – 800 nm, 100 mW/ cm^2) for 0, 1, 3, and 6 min, respectively. The fluorescence intensity of DCF was detected with the confocal microscopy by collecting the signal between 500 and 525 nm at λ_{ex} = 488 nm.

2.11 Apoptosis study

Annexin V-FITC and Hoechst staining. Apoptosis induced by complex NIR-Ir-XE under light and dark conditions was tested by confocal microscopy. MCF-7 cells were incubated with 5 μ M NIR-Ir-XE for 1 h and then the cells were irradiated by a xenon lamp (400 – 800 nm, 100 mW/ cm^2) for 10 min. Then the cells were incubated for another 5 h and stained with Annexin V-FITC and then with Hoechst 33342 for 15 min in the dark at room temperature. Confocal microscopy was used to collect the fluorescence intensity from the cells (Annexin V-FITC, λ_{ex} = 488 nm, λ_{em} = 500–560 nm; Hoechst 33342, λ_{ex} = 405 nm, λ_{em} = 440–480 nm).

JC-1 dye staining. A fresh 200 μ M JC-1 dye stock solution was prepared in DMSO. MCF-7 cells were incubated with 5 μ M NIR-Ir-XE for 1 h and then the cells were irradiated by a xenon lamp (400 – 800 nm, 100 mW/ cm^2) for 1, 5, and 10 min, respectively. Then, the cell culture medium was removed and then it was replaced with a warm medium PBS. The cells were washed once by adding PBS and the fresh cell culture medium

RPMI 1640 again. 2 μM (final concentration) of JC-1 dye was added and the cells were incubated at 37°C and 5% CO_2 for 20 min. The culture medium of all samples was removed and the cells were washed once by adding warm PBS. Confocal microscopy was used to collect the fluorescence intensity from the cells ($\lambda_{\text{ex}} = 515 \text{ nm}$, $\lambda_{\text{em}} = 530 - 560 \text{ nm}$).

2.12 Tumor-bearing mouse model and anticancer studies

This study was performed with the Institutional Animal Care and Use Committee of The Hong Kong Polytechnic University, and animals received care in accordance with the Guidance Suggestions for the Care and Use of Laboratory Animals. The MCF-7 tumor models were successfully established by subcutaneous injection into the right thigh of each six-week-old BALB/c nude mouse with ~ 100 million Hela cells suspended in 100 μL PBS.

When the tumors had reached an average volume of 80 mm^3 , mice ($n = 3$) were injected with saline (100 μL) or NIR-Ir-XE (100 μL , 3 mg/Kg) separately. A xenon lamp light source system was used to irradiate the tumors for 25 min for two times at 1 day and 2 days after injection. The growth of the tumor was measured with a caliper every 2 days during the period of treatment (14 days) and the volume was calculated (volume = length \times width² \times 0.5).

3. Results and discussion

3.1 Synthesis of iridium(III) complexes

Research work has reported that the long-lived ³IL excited state of metal-based PSs can be achieved by π -conjugated ligands, such as an xanthene dye.^[49] Thus, two luminescent Ir(III) complexes of the type $[\text{Ir}(\text{C}^{\wedge}\text{N})_2(\text{N}^{\wedge}\text{N})][\text{PF}_6]$ (Scheme 2) [$\text{HC}^{\wedge}\text{N} = \text{btpq}$; $\text{N}^{\wedge}\text{N} = \text{XE-P}$ and bpy] were designed and synthesized to investigate the effect of the production of the xanthene dye on singlet oxygen (¹O₂).

The xanthene appended ligand, XE-P, was prepared by the reaction of 4'-methyl-[2,2'-bipyridine]-4-carbaldehyde (compound P) and compound XE. The complex NIR-Ir-XE was synthesized via the reaction of XE-P with $[\text{Ir}(\text{btpq})_2\text{Cl}]_2$, and it was obtained as a dark purple solid after purification by silica column chromatography. As a control complex, NIR-Ir-bpy, in which the xanthene part was absent, was also synthesized. The newly synthesized ligand btpq, XE-P, NIR-Ir-bpy and NIR-Ir-XE have been characterized by ¹H NMR, ¹³C NMR and high-resolution mass spectroscopy (HR-MS) (Figs. S14-S25). The positive ion ESI mass spectra displayed the $[\text{M-PF}_6]^+$ signals with the expected isotopic distribution pattern for all Ir(III) complexes.

3.2 Photophysical properties of NIR-Ir-XE

The UV-vis absorption spectra of XE-P, NIR-Ir-bpy, and NIR-Ir-XE in ethanol are shown in Figs. 1, S1, and S2 and their photophysical data are summarized in Table 1. The XE-P ligand shows an intense absorption at 541 nm, assignable to the characteristic π - π^* intraligand (IL) transition of the xanthene dye. For complexes NIR-Ir-bpy and NIR-Ir-XE, the sharp and

narrow absorption bands in the region of 250 – 380 nm were assigned to the π – π^* transitions centered on the $\text{N}^{\wedge}\text{N}$ and $\text{C}^{\wedge}\text{N}$ ligands, and another low-energy band between 430 – 650 nm was assigned to the charge transfer (CT) transitions, such as the metal-to- $\text{C}^{\wedge}\text{N}$ ligand charge transfer (MLCT) and $\text{C}^{\wedge}\text{N}$ ligand to $\text{N}^{\wedge}\text{N}$ ligand charge transfer (LLCT) transitions.^[50]

The emission spectrum of XE-P shows an intense emission peak at 545 nm in ethanol with a quantum yield (Φ_{em}) of 0.183, and this emission is originated from the singlet IL excited state of the xanthene unit. For NIR-Ir-bpy and NIR-Ir-XE, they give a similar emission at around 650 nm (a shoulder peak at around 705 nm) with a quantum yield of 0.013 and 0.030, respectively. It should be noted that the absorption and emission bands for NIR-Ir-XE were extended with tails at 650 nm and 820 nm, respectively, favoring the low energy excitation and high signal-to-noise fluorescence imaging (Table S1).

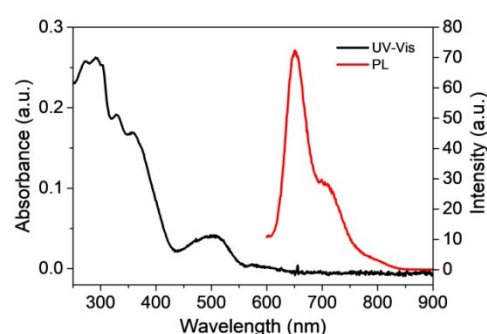


Fig. 1 The absorption and phosphorescence spectra of complex NIR-Ir-XE at $\lambda_{\text{ex}} = 500 \text{ nm}$.

Table 1. Photophysical data of XE-P, NIR-Ir-bpy, and NIR-Ir-XE

Sample	Solvent	$\lambda_{\text{abs,peak}}/\text{nm}$	$\lambda_{\text{PL,peak}}/\text{nm}$	Φ_{em}	τ/ns
XE-P	$\text{C}_2\text{H}_5\text{OH}$	270, 541	545	0.183	1.5
NIR-Ir-bpy	$\text{C}_2\text{H}_5\text{OH}$	305, 356, 508	651, 705	0.018	408
NIR-Ir-XE	$\text{C}_2\text{H}_5\text{OH}$	293, 356, 510	652, 704	0.030	603

3.3 Density functional theory calculations

For a better understanding of the influence of xanthene on the photophysical properties of NIR-Ir-XE, DFT and TD-DFT calculations were performed for XE-P and NIR-Ir-XE. The calculated HOMO and LUMO distributions are shown in Figs. 2 and S3, and the calculated frontier molecular orbital energies of XE-P and NIR-Ir-XE are shown in Table S2. Moreover, vertical absorption energies and the corresponding oscillator strengths of NIR-Ir-XE are shown in Table S3. As shown in Fig. 2, for NIR-Ir-XE, the HOMO primarily resides on the main ligand btpq and iridium center, while the LUMO, LUMO+1 and LUMO+2 are delocalized on the auxiliary XE-P moiety, which indicates that the T_1 state for NIR-Ir-XE can be regulated by the ³IL excited state on the xanthene unit in this system. The introduction of the xanthene unit into the $\text{N}^{\wedge}\text{N}$ ligand leads to the lower LUMO energy level, which may reduce the singlet-triplet gap of NIR-Ir-XE. On the other hand, the computational studies of the free ligand XE-P on the singlet energy at 2.55 eV were also

made (Fig. S3). The calculated XE-P singlet energy is in line with its observed absorption and fluorescence energies.

3.4 Quantum yields for $^1\text{O}_2$ generation

Typically, triplet excited state lifetime (τ_T) of metal complex is a crucial factor for the generation of $^1\text{O}_2$. The transient absorption (TA) of NIR-Ir-XE in degassed toluene was studied. As shown in Fig. S4, a transient absorption signal from 420 nm extended to a near-infrared region (~ 750 nm) was monitored from 278 ns to 1112 ns. It is therefore inferred that NIR-Ir-XE has a relatively long triplet excited state lifetime, which is beneficial to increase the yield of $^1\text{O}_2$.

The efficient ROS generation capability of a photosensitizer upon light irradiation is the pivotal step of PDT. Thus, the singlet oxygen ($^1\text{O}_2$) generation ability of NIR-Ir-XE in PBS was evaluated by measuring the photodegradation rate of 9,10-anthracenediyl-bis(methylene)-dimalonic acid (ABDA). As displayed in Figs. 3 and S5, the absorptions at 358, 379, and 402 nm ascribed to the anthracene moiety in ABDA gradually weakened when the mixed solution of NIR-Ir-XE and ABDA was exposed to light irradiation (532 nm) (Fig. 3a), indicating the formation of $^1\text{O}_2$. To compare the $^1\text{O}_2$ generation efficiency of NIR-Ir-bpy, the decomposition rate of ABDA in the presence of NIR-Ir-bpy was tested under the same conditions. Results in Fig. 3b indicated that, upon light irradiation, the decomposition rate of ABDA is slower than that of NIR-Ir-XE. The generation quantum yields of $^1\text{O}_2$ for NIR-Ir-bpy and NIR-Ir-XE were obtained as 0.29 and 0.72, respectively. As another control group, the decomposition rates of ABDA by ligand XE-P was also tested, and it was found that the $^1\text{O}_2$ quantum yield is very low for compound XE-P (Fig. S6). All these data suggested that NIR-Ir-XE exhibits higher $^1\text{O}_2$ generation efficiency than that of the control complex NIR-Ir-bpy.

Furthermore, in order to identify the type of ROS produced by NIR-Ir-XE, electron spin resonance spectroscopy (ESR) was conducted using 2,2,6,6-tetramethyl-4-piperidinol (a TEMP reagent) as the $^1\text{O}_2$ trapping agent. As shown in Fig. 3d, characteristic $^1\text{O}_2$ -induced triplet of signals was observed when NIR-Ir-XE (10 μM) was mixed with TEMP (100 mM) and irradiated for 6 min (400 – 800 nm, 50 mW cm^{-2}), suggesting that $^1\text{O}_2$ was formed.^[51] On the contrary, no signals could be detected without light irradiation. Likewise, no peaks were observed for the blank group without NIR-Ir-XE.

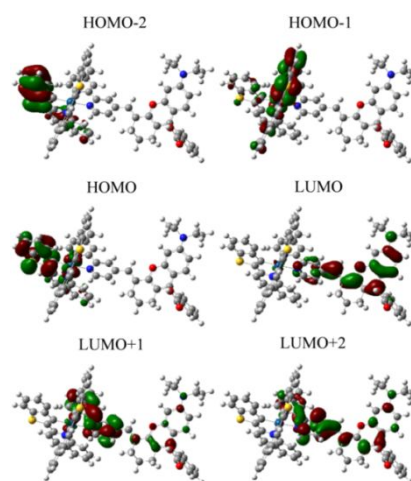


Fig. 2 Representations of the frontier molecular orbitals (MOs) for the S_0 geometry of NIR-Ir-XE at the B3LYP/[LANL2DZ-ECP/6-31G*] level.

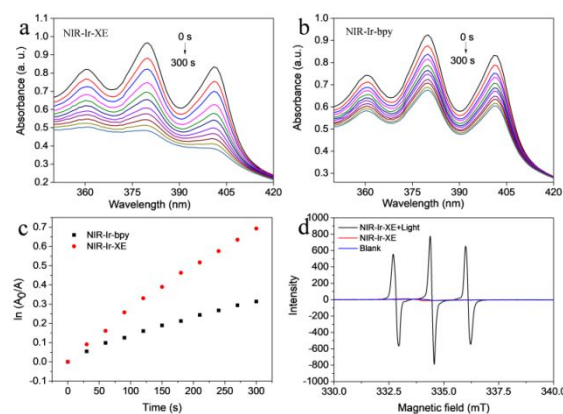


Fig. 3 The decomposition rates of ABDA by NIR-Ir-XE and NIR-Ir-bpy (a-c), A_0 and A are the absorbance of ABDA in the presence of the photosensitizers at 532 nm before and after irradiation, respectively. The absorbance value of NIR-Ir-bpy and NIR-Ir-XE at 532 nm is 0.167 and 0.156, respectively. (d) Electron spin resonance spectroscopy (ESR) signals obtained upon irradiation (400–800 nm, 50 mW cm^{-2}) for 5 min of $\text{H}_2\text{O}/\text{CH}_3\text{CN}$ (8/2, v/v) solutions of 100 mM 2,2,6,6-tetramethyl-4-piperidinol (a TEMP reagent) and 10 μM NIR-Ir-XE.

3.5 In vitro PDT studies

It is essential for PDT to possess low toxicity in dark, but high toxicity upon light irradiation. We used a standard MTT cell viability assay to study the cytotoxicity of NIR-Ir-XE. The complex NIR-Ir-XE showed negligible toxicity to MCF-7 cells in dark condition, whereas the significant dose-dependent cytotoxicity of NIR-Ir-XE upon light irradiation was observed in MCF-7 cells. As shown in Fig. 4, the cell viability of MCF-7 cells is higher than 80% in all concentration groups under dark condition (0 min), while the cell viability decreased to 32% when incubation of NIR-Ir-XE (10 μM) upon white light was irradiated for 15 min.

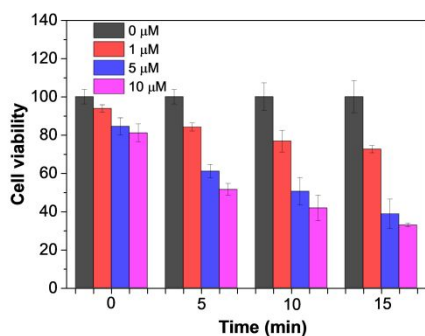


Fig. 4 Cytotoxicity of the NIR-Ir-XE-incubated MCF-7 cells with different concentrations (0, 1, 5, and 10 μM) and irradiation time (0, 5, 10, and 15 min) under light irradiation (400–800 nm).

3.6 Staining mitochondria with high photostability

In order to investigate the intracellular localization of NIR-Ir-XE, MCF-7 cells have been co-stained with the mitochondria-specific probe, Mito-Tracker Green FM (MTG). Confocal microscopy shows that most of them are specifically localized in the mitochondria, suggesting that the modified xanthenes ligand and NIR-Ir-XE retain the mitochondria-targeting ability (Fig. 5). According to the overlapping of fluorescence signals between NIR-Ir-XE and MTG, the complex NIR-Ir-XE is essentially localized in the mitochondria (Fig. 5c). We compared the mitochondrial targeting ability by capturing the co-localization images between NIR-Ir-XE and commercially available MTG in MCF-7 cells. As shown in Figs. 5f and S7, the red fluorescence of NIR-Ir-XE overlapped with the green fluorescence of MTG with the average Pearson's correlation coefficient (R) of 0.935. It is interesting to note that the incorporation of Ir(III) complex into the xanthenes-tethered ligand results in stronger mitochondria-targeting properties, probably because of the balanced interplay between the cationic charge and lipophilicity.

Photostability is very critical for long-time tracking in disease diagnostics. In particular, the multiple image acquisition cycles and prolonged light exposure of probes may result in serious photobleaching and image distortion. Hence, the photostability of NIR-Ir-XE in ethanol solution was tested; the luminescence intensity of NIR-Ir-XE was nearly unchanged after irradiation at 500 nm for 30 min (Fig. S8), indicating that the NIR-Ir-XE has excellent photostability. Second, the photostability study of NIR-Ir-XE versus commercial fluorescent dye Mito-Tracker Red (MTR) in cell imaging was conducted in detail. Here the photostability test was conducted in intracellular environment (Fig. 6a). After sequentially scanning for 30 s in living MCF-7 cells, the fluorescent signal of MTR almost disappeared, whereas NIR-Ir-XE still kept 90% of the initial value (Fig. 6b). Even after 30 scans, the relatively slight decrease of NIR-Ir-XE further confirmed its excellent photostability for bioimaging.

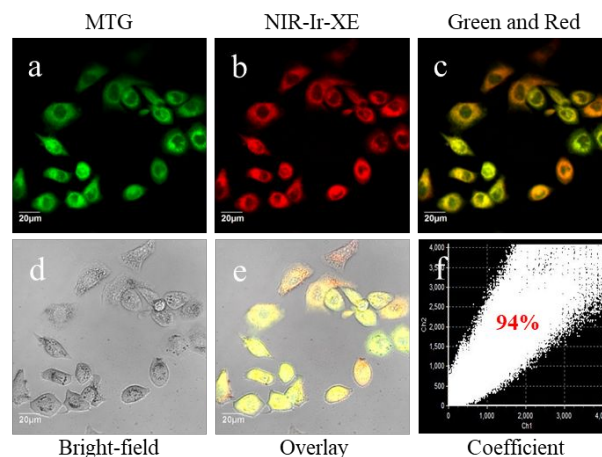


Fig. 5 Confocal images of MCF-7 cells with the incubation of NIR-Ir-XE (5 μM) for 30 minutes followed by co-staining with Mito-Tracker Green FM (MTG, 100 nM) for 30 min. (a) green channel of MTG; (b) Red channel of NIR-Ir-XE; (c) overlaid of green and red channels; (d) bright-field; (e) overlaid of green, red, and bright-field channels; (f) Pearson's correlation coefficients of green and red channels. Imaging conditions: Green channels of MTG, $\lambda_{\text{ex}} = 488 \text{ nm}$, $\lambda_{\text{em}} = 505 - 550 \text{ nm}$; red channels of NIR-Ir-XE, $\lambda_{\text{ex}} = 532 \text{ nm}$, $\lambda_{\text{em}} = 630 - 730 \text{ nm}$.

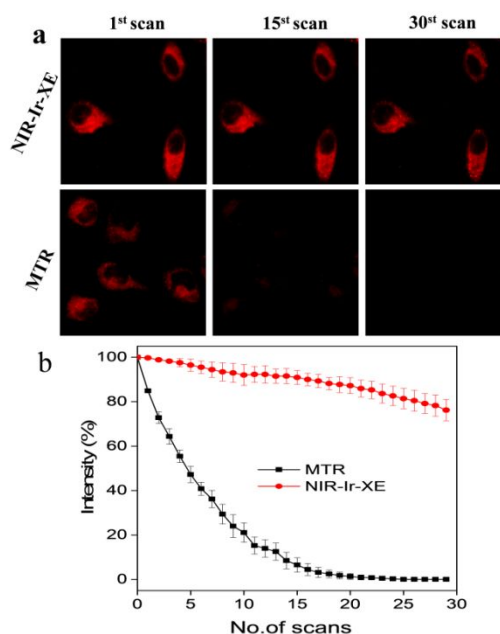


Fig. 6 (a) Confocal images of MCF-7 cells stained with NIR-Ir-XE and Mito-Tracker Red (MTR) at different scan times. (b) Excellent photostability of NIR-Ir-XE. The fluorescence signal loss (%) profiles of NIR-Ir-XE and MTR. Emission signal was normalized to the maximum intensity at the beginning of irradiation ($n = 3$, data expressed as average \pm standard deviation).

3.7 Cell ROS imaging of NIR-Ir-XE

In cellular ROS generation, we further utilized the non-fluorescent agent of dichlorofluorescein diacetate (DCF-DA) as the indicator for detecting ROS by-products of singlet oxygen generation. Upon addition of NIR-Ir-XE with light irradiation, the strong fluorescence from the oxidized DCF-DA was observed in the green channel with increasing time from 1 to 6

min (Fig. 7). As a control group, using the MCF-7 cells without NIR-Ir-XE, no obvious increase in fluorescence was observed (Fig. S9), while in those treated with NIR-Ir-XE, fluorescence was observed (Fig. 7), indicating that NIR-Ir-XE can generate ROS inside MCF-7 cells. As another control group, we have measured the ROS generation in MCF-7 cells with complex NIR-Ir-bpy (Fig. S10). The green fluorescence signal from the cells incubated with NIR-Ir-bpy is weak, indicating that NIR-Ir-bpy has a low PDT activity.

As an efficiently consuming species of ROS, vitamin C (Vc) was added to verify this ROS generation. Clearly, it was found that DCF-DA still maintained the initial nonfluorescent state in the presence of NIR-Ir-XE under light irradiation (Fig. 8). Therefore, NIR-Ir-XE efficiently generated $^1\text{O}_2$ in endogenous MCF-7 cells, also indicative of a potential light-induced ROS agent.

3.8 Study of cell apoptosis with NIR-Ir-XE

On the basis of the results of the intracellular ROS production and colocalization study, it is reasonable to anticipate that the ROS is essentially generated within the mitochondria. To study the apoptotic development in PDT action, MCF-7 cells were incubated with NIR-Ir-XE and irradiated with 400–800 nm. Following the irradiation, the treated cells were immediately incubated with Annexin V-FITC (fluorescein isothiocyanate) for 30 min. A fluorescent probe Annexin V-FITC was selected to distinguish viable cells from apoptotic ones since Annexin V can bind to the membrane of apoptotic cell that expresses phosphatidylserine. As shown in Fig. 9, for MCF-7 cells irradiated with 400 – 800 nm after 10 min, a majority of the cells are apoptotic. However, no green fluorescence (from FITC) was detected in cells incubated without NIR-Ir-XE or light irradiation (Fig. S11). As another control group, cell apoptosis experiment in response to PDT of NIR-Ir-bpy was also tested. As shown in Fig. S12, only a weak green fluorescence (from FITC) was observed, indicating that the PDT activity of NIR-Ir-bpy is not good.

JC-1 is a novel cationic carbocyanine dye that accumulates in mitochondria. Mitochondrial depolarization occurs as a result of mitochondrial dysfunction and is commonly regarded as a hallmark of apoptosis. The J-aggregate form of JC-1 with intense red fluorescence is formed in healthy cells with high $\Delta\Psi_m$, while the green fluorescent monomeric form exists in the apoptotic cells with low $\Delta\Psi_m$. These characteristics make JC-1 a sensitive marker for mitochondrial membrane potential. In order to confirm that the mechanism of cell death arises from the photocytotoxicity of NIR-Ir-XE, MCF-7 cells were incubated with NIR-Ir-XE and irradiated with light. Following the irradiation, the treated cells were immediately incubated with JC-1 dye for 6 min. As shown in Fig. 10, for MCF-7 cells irradiated with light after 6 min, a dramatic increase in the green fluorescence was observed for the MCF-7 cells treated with NIR-Ir-XE upon irradiation. This strongly indicates an increase in mitochondrial depolarization and hence apoptosis, which is responsible for the photocytotoxicity of NIR-Ir-XE.

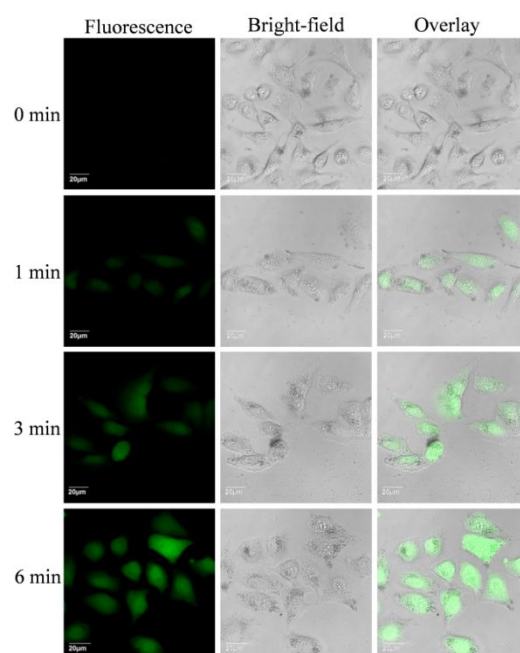


Fig. 7 ROS generation in MCF-7 cells with NIR-Ir-XE (5 μM). Confocal laser scanning microscopy images showing the ROS generation in MCF-7 cells with light irradiation (0, 1, 3, and 6 min) after treatment with DCF-DA. The green fluorescence is from DCF-DA ($\lambda_{\text{ex}} = 488 \text{ nm}$, $\lambda_{\text{em}} = 505 - 525 \text{ nm}$).

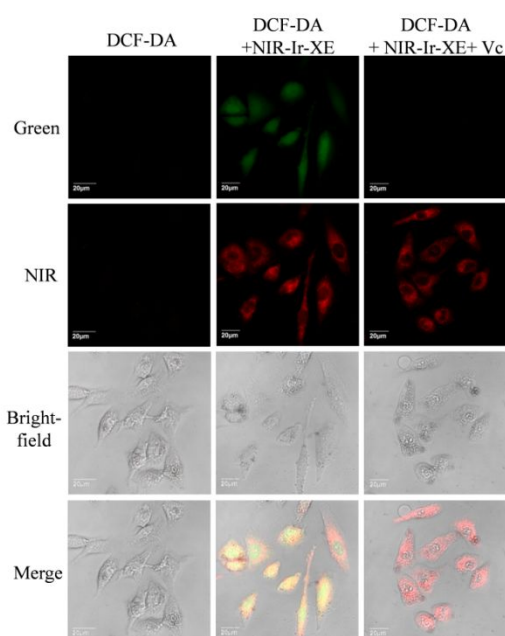


Fig. 8 Confocal images showing the ROS generation in MCF-7 cells with light irradiation (100 mW cm^{-2} , 5 min) after treatment with DCF-DA. The green fluorescence is from DCF-DA ($\lambda_{\text{ex}} = 488 \text{ nm}$, $\lambda_{\text{em}} = 505 - 525 \text{ nm}$). The NIR fluorescence is from NIR-Ir-XE ($\lambda_{\text{ex}} = 532 \text{ nm}$, $\lambda_{\text{em}} = 630 - 730 \text{ nm}$).

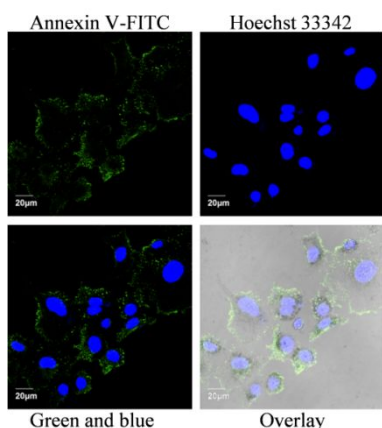


Fig. 9 Apoptosis development in response to PDT of NIR-Ir-XE. MCF-7 cells incubated with NIR-Ir-XE (5 μM) were irradiated for 10 min (100 mW cm^{-2}). Imaging conditions: Fluorescein isothiocyanate (FITC)-tagged Annexin V ($\lambda_{\text{ex}} = 488 \text{ nm}$, $\lambda_{\text{em}} = 510 - 540 \text{ nm}$) and Hoechst 33342 ($\lambda_{\text{ex}} = 405 \text{ nm}$, $\lambda_{\text{em}} = 440 - 480 \text{ nm}$).

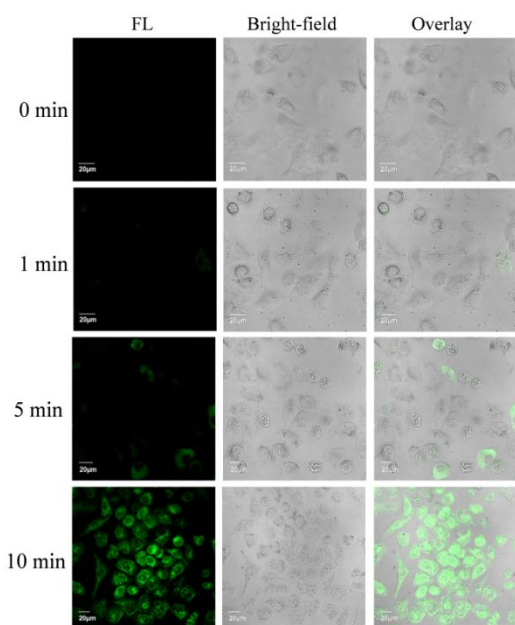


Fig. 10 Apoptosis development in response to PDT of NIR-Ir-XE (5 μM). MCF-7 cells incubated with NIR-Ir-XE were irradiated (100 mW cm^{-2}) for 0, 1, 5, and 10 min, respectively. Imaging conditions: JC-1 dye, $\lambda_{\text{ex}} = 515 \text{ nm}$, $\lambda_{\text{em}} = 530 - 560 \text{ nm}$.

3.9 In vivo antitumor efficacy studies

Encouraged by the good performance of NIR-Ir-XE in cellular experiments, its potential for tumor inhibition was investigated *in vivo*. The murine models were established by subcutaneously injecting MCF-7 cells. To distinguish the roles played by the light source, oxygen and photosensitizer, the tumor-bearing mice were then randomly divided into four groups. The tumor volume and mice body weight were continuously recorded every two days. Tumor-bearing mice were injected with PBS (control group), with PBS and light (532 nm, 100 mW cm^{-2} , 15 min) (light group), with NIR-Ir-XE (dark group), and with NIR-Ir-XE and light (PDT group). As shown in Fig. 11b, in the control and light groups, the relative tumor volumes showed an obvious increase after 14 days, suggesting

that only irradiation has no evident impact on the tumor growth. Then, NIR-Ir-XE was intratumorally injected into the tumor tissue followed by different treatments in dark groups and PDT groups. NIR-Ir-XE-treated mice in the dark group exhibited a similar tumor growth to the control group owing to the low photocytotoxicity of NIR-Ir-XE without light. In contrast, a slight change of tumor volume in the group PDT mice indicated the good antitumor performance of NIR-Ir-XE under light irradiation (Fig. 11b), which is significantly different from the control groups, and the experimental photographs of tumors excised from the representative mice visually reveal the tumor size after treatment with NIR-Ir-XE (Fig. 11c). Histology results of the mice injected with NIR-Ir-XE have been studied as well. By utilizing the hematoxylin and eosin (H&E) staining method, tumor tissue necrosis was clearly observed in the PDT group (Fig. 11d). These results confirm the excellent PDT effect for killing tumors induced by NIR-Ir-XE.

Furthermore, the systemic toxicity of various treatments was evaluated via the mice's body weight changes and the histological slices. In comparison with the control group, negligible bodyweight losses were observed in light, dark, and PDT groups (Fig. 11a). No pathological changes were found in the liver, heart, spleen, kidney, and lung in the four groups (Fig. S13), indicating that NIR-Ir-XE has no significant side effects on the healthy mice, confirming the favorable biocompatibility of NIR-Ir-XE *in vivo*. These results reveal that NIR-Ir-XE is suitable for *in vivo* PDT applications.

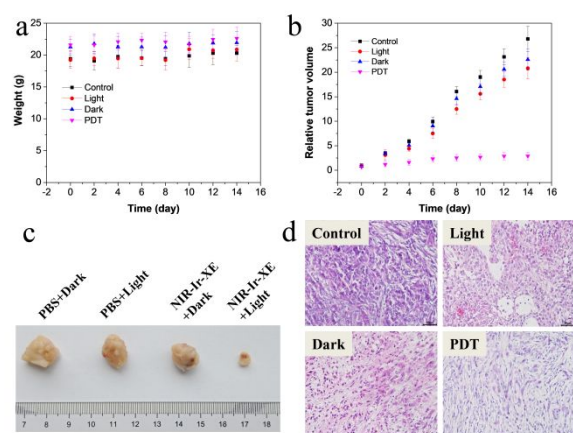


Fig. 11 Body weight of mice with different treatments with prolonged treatment time (a) and tumor volume (b) of four groups after individual treatments. Photos of harvested tumors from mice in different groups after 14 days of treatment (c) and H&E analysis of tumor tissue from different groups after 14 days of treatment (d), scale bar: 50 μm .

4. Conclusions

In summary, we have established a simple strategy to design and develop a new photosensitizer agent based on the conjugation of a cyclometalated Ir(III) complex to an xanthene dye to afford mitochondria-targeting photosensitizer (NIR-Ir-XE). Xanthene dye triplet excited states in such NIR-Ir-XE system, which are involved in $^1\text{O}_2$ formation, can be generated. The combination of the xanthenes dye and phosphorescent

Ir(III) center exhibits the synergistic merits for the PDT applications, including low dark cytotoxicity, selective mitochondria-targeting uptake, high molar absorptivity, and high photostability. Evidence of apoptotic cell death, which is consistent with their mitochondrial localization property, was also seen in the photocytotoxicity induced by NIR-Ir-XE. Overall, these properties indicate that conjugation between xanthene dye and highly potent NIR-emitting Ir(III) complex can be exploited to overcome some of the drawbacks of traditional PSs, such as low $^1\text{O}_2$ generation efficiency and poor tissue penetration. These properties qualify NIR-Ir-XE as a highly promising PDT agent. This study offers a new method to improve the efficiency of photosensitizers for clinical cancer treatment. Work is in progress in our laboratory to develop novel Ir(III)-fluorophore conjugates operating in the phototherapeutic window with the aim of using them in targeted PDT.

Conflicts of interest

There are no conflicts to declare.

Acknowledgements

This work was financially supported by the National Natural Science Foundation of China (51873176 and 21967001), Hong Kong Research Grants Council (PolyU153058/19P), Guangdong-Hong Kong-Macao Joint Laboratory of Optoelectronic and Magnetic Functional Materials (2019B121205002), the Hong Kong Polytechnic University (1-ZE1C), Ms Clarea Au for the Endowed Professorship in Energy (847S), and the Double-Thousand Talents Plan of Jiangxi Province (2019). Y. Wu *et al.* also gratefully acknowledges Prof. Huifang Li of Qingdao University of Science and Technology for the support of DFT calculation.

Notes and references

- D. E. J. G. J. Dolmans, D. Fukumura and R. K. Jain, *Nat. Rev. Cancer*, 2003, **3**, 380-387.
- P. Agostinis, K. Berg, K. A. Cengel, T. H. Foster, A. W. Girotti, S. O. Gollnick, S. M. Hahn, M. R. Hamblin, A. Juzeniene, D. Kessel, M. Korbelik, J. Moan, P. Mroz, D. Nowis, J. Piette, B. C. Wilson and J. Golab, *CA-Cancer J. Clin.*, 2011, **61**, 250-281.
- S. S. Lucky, K. C. Soo and Y. Zhang, *Chem. Rev.*, 2015, **115**, 1990-2042.
- C. Mari, V. Pierroz, S. Ferrari and G. Gasser, *Chem. Sci.*, 2015, **6**, 2660-2686.
- W. Fan, P. Huang and X. Chen, *Chem. Soc. Rev.*, 2016, **45**, 6488-6519.
- A. Sasnauskienė, J. Kadziauskas, N. Vezelyte, V. Jonusiene and V. Kirveliėne, *Apoptosis*, 2009, **14**, 276-286.
- Y. Yu, Q. Xu, S. He, H. Xiong, Q. Zhang, W. Xu, V. Ricotta, L. Bai, Q. Zhang, Z. Yu, J. Ding, H. Xiao and D. Zhou, *Coord. Chem. Rev.*, 2019, **387**, 154-179.
- F. Hu, S. Xu and B. Liu, *Adv. Mater.*, 2018, **30**, 1801350.
- H. Huang, S. Banerjee and P. J. Sadler, *ChemBioChem*, 2018, **19**, 1574-1589.
- L. K. McKenzie, H. E. Bryant and J. A. Weinstein, *Coord. Chem. Rev.*, 2019, **379**, 2-29.
- H. He, S. Ji, Y. He, A. Zhu, Y. Zou, Y. Deng, H. Ke, H. Yang, Y. Zhao, Z. Guo and H. Chen, *Adv. Mater.*, 2017, **29**, 1606690.
- B. Yu, H. Wei, Q. He, C. A. Ferreira, C. J. Kuttyreff, D. Ni, Z. T. Rosenkrans, L. Cheng, F. Yu, J. W. Engle, X. Lan and W. Cai, *Angew. Chem. Int. Ed.*, 2018, **57**, 218-222.
- R. Wang, X. Gu, Q. Li, J. Gao, B. Shi, G. Xu, T. Zhu, H. Tian and C. Zhao, *J. Am. Chem. Soc.*, 2020, **142**, 15084-15090.
- Y. You and W. Nam, *Chem. Soc. Rev.*, 2012, **41**, 7061-7084.
- M. T. Whited, P. I. Djurovich, S. T. Roberts, A. C. Durrell, C. W. Schlenker, S. E. Bradforth and M. E. Thompson, *J. Am. Chem. Soc.*, 2011, **133**, 88-96.
- J. Zhao, W. Wu, J. Sun and S. Guo, *Chem. Soc. Rev.*, 2013, **42**, 5323-5351.
- G. Li, M. F. Mark, H. Lv, D. W. McCamant and R. Eisenberg, *J. Am. Chem. Soc.*, 2018, **140**, 2575-2586.
- H. Huang, B. Yu, P. Zhang, J. Huang, Y. Chen, G. Gasser, L. Ji and H. Chao, *Angew. Chem. Int. Ed.*, 2015, **54**, 14049-14052.
- J. Karges, S. Kuang, F. Maschietto, O. Blacque, I. Ciofini, H. Chao and G. Gasser, *Nat. Commun.*, 2020, **11**, 3262.
- W. Lv, Z. Zhang, K. Y. Zhang, H. Yang, S. Liu, A. Xu, S. Guo, Q. Zhao and W. Huang, *Angew. Chem. Int. Ed.*, 2016, **55**, 9947-9951.
- K. Y. Zhang, P. Gao, G. Sun, T. Zhang, X. Li, S. Liu, Q. Zhao, K. K.-W. Lo and W. Huang, *J. Am. Chem. Soc.*, 2018, **140**, 7827-7834.
- J. Jiang, Y. Qian, Z. Xu, Z. Lv, P. Tao, M. Xie, S. Liu, W. Huang and Q. Zhao, *Chem. Sci.*, 2019, **10**, 5085-5094.
- L. He, Y. Li, C.-P. Tan, R.-R. Ye, M.-H. Chen, J.-J. Cao, L.-N. Ji and Z.-W. Mao, *Chem. Sci.*, 2015, **6**, 5409-5418.
- F.-X. Wang, M.-H. Chen, Y.-N. Lin, H. Zhang, C.-P. Tan, L.-N. Ji and Z.-W. Mao, *ACS Appl. Mater. Interfaces*, 2017, **9**, 42471-42481.
- L. He, M.-F. Zhang, Z.-Y. Pan, K.-N. Wang, Z.-J. Zhao, Y. Li and Z.-W. Mao, *Chem. Commun.*, 2019, **55**, 10472-10475.
- H. Xiang, H. Chen, H. P. Tham, S. Z. F. Phua, J.-G. Liu and Y. Zhao, *ACS Appl. Mater. Interfaces*, 2017, **9**, 27553-27562.
- R. Bevernaegie, B. Doix, E. Bastien, A. Diman, A. Decottignies, O. Feron and B. Elias, *J. Am. Chem. Soc.*, 2019, **141**, 18486-18491.
- Q. Yang, H. Jin, Y. Gao, J. Lin, H. Yang and S. Yang, *ACS Appl. Mater. Interfaces*, 2019, **11**, 15417-15425.
- S. Yi, Z. Lu, J. Zhang, J. Wang, Z. Xie and L. Hou, *ACS Appl. Mater. Interfaces*, 2019, **11**, 15276-15289.
- L. Zhang, Y. Li, W. Che, D. Zhu, G. Li, Z. Xie, N. Song, S. Liu, B. Z. Tang, X. Liu, Z. Su and M. R. Bryce, *Adv. Sci.*, 2019, **6**, 1802050.
- C. Li, X. Zheng, W. Chen, S. Ji, Y. Yuan and X. Jiang, *Nano Lett.*, 2020, **20**, 6526-6534.
- J. Zhao, X. Zhang, L. Fang, C. Gao, C. Xu and S. Gou, *Small*, 2020, **16**, 2000363.
- C. Liu, L. Zhou, F. Wei, L. Li, S. Zhao, P. Gong, L. Cai and K. M.-C. Wong, *ACS Appl. Mater. Interfaces*, 2019, **11**, 8797-8806.
- X. Chen, T. Pradhan, F. Wang, J. S. Kim and J. Yoon, *Chem. Rev.*, 2012, **112**, 1910-1956.
- Y. Yang, Q. Zhao, W. Feng and F. Li, *Chem. Rev.*, 2013, **113**, 192-270.
- W. Xu, Z. Zeng, J.-H. Jiang, Y.-T. Chang and L. Yuan, *Angew. Chem. Int. Ed.*, 2016, **55**, 13658-13699.
- X. Jiao, Y. Li, J. Niu, X. Xie, X. Wang and B. Tang, *Anal. Chem.*, 2018, **90**, 533-555.
- Q. Zhang and K. M.-C. Wong, *Coord. Chem. Rev.*, 2020, **416**, 213336.
- J. E. Hill, M. K. Linder, K. S. Davies, G. A. Sawada, J. Morgan, T. Y. Ohulchanskyy and M. R. Detty, *J. Med. Chem.*, 2014, **57**, 8622-8634.
- V. Novohradsky, A. Rovira, C. Hally, A. Galindo, G. Viguera, A. Gandioso, M. Svitelova, R. Bresolí-Obach, H. Kostrhunova, L.

- Markova, J. Kasparikova, S. Nonell, J. Ruiz, V. Brabec and V. Marchán, *Angew. Chem. Int. Ed.*, 2019, **58**, 6311-6315.
- 41 R. Weissleder, *Nat. Biotechnol.*, 2001, **19**, 316-317.
- 42 H. Chen, X. Zeng, H. P. Tham, S. Z. F. Phua, W. Cheng, W. Zeng, H. Shi, L. Mei and Y. Zhao, *Angew. Chem. Int. Ed.*, 2019, **58**, 7641-7646.
- 43 D. Wang, M. M. S. Lee, G. Shan, R. T. K. Kwok, J. W. Y. Lam, H. Su, Y. Cai and B. Z. Tang, *Adv. Mater.*, 2018, **30**, 1802105.
- 44 L. Yuan, W. Lin, Y. Yang and H. Chen, *J. Am. Chem. Soc.*, 2012, **134**, 1200-1211.
- 45 C. Adamo and V. Barone, *J. Chem. Phys.*, 1999, **110**, 6158-6170.
- 46 H. Li, P. Winget, C. Risko, J. S. Sears and J.-L. Brédas, *Phys. Chem. Chem. Phys.*, 2013, **15**, 6293-6302.
- 47 P. J. Hay and W. R. Wadt, *J. Chem. Phys.*, 1985, **82**, 299-310.
- 48 S. Fantacci, F. De Angelis and A. Selloni, *J. Am. Chem. Soc.*, 2003, **125**, 4381-4387.
- 49 X. Guo, Q. Chen, Y. Tong, Y. Li, Y. Liu, D. Zhao and Y. Ma, *J. Phys. Chem. A*, 2018, **122**, 6963-6969.
- 50 Q. Zhao, F. Li and C. Huang, *Chem. Soc. Rev.*, 2010, **39**, 3007-3030.
- 51 G. Nardi, I. Manet, S. Monti, M. A. Miranda and V. Lhiaubet-Vallet, *Free Radical Bio.Med.*, 2014, **77**, 64-70.